ACS OMEGA

http://pubs.acs.org/journal/acsodf

Article

Specific Tumor Cell Detection by a Metabolically Targeted Aggregation-Induced Emission-Based Gold Nanoprobe

Xiaohan Kong,† Yangwen Sun,† Qian Zhang, Siju Li, Yizhen Jia, Rui Li, Yang Liu,* and Zhiyong Xie*

Cite This: *ACS Omega* 2022, 7, 18073−18084

Read Online

ACCESS | Metrics & More | Article Recommendations | Supporting Information

ABSTRACT: Detection of circulating tumor cells (CTCs) could be widely used for early diagnosis and real-time monitoring of tumor progression in liquid biopsy samples. Compared with normal cells, tumor cells exhibit relatively strong negative surface charges due to the high rate of glycolysis. In this study, a cationic fluorescence "turn-on" aggregation-induced emission (AIE) nanoprobe based on gold nanorods (GNRs) was designed and tested to detect tumor cells specifically. In brief, tetraphenylethene (TPE), an AIE dye, was conjugated to the cationic polymer polyethylenimine (PEI) yielding TPEI. TPEI-PEG-SH was obtained by further functionalizing TPEI with a thiol group. TPEI-PEG-SH was grafted to the surface of GNRs, yielding the cationic AIE nanoprobe, named as GNRs-PEG-TPEI. The nanoprobe was characterized to have a uniform particle size of 172 nm, a strong positive surface charge (+54.87 mV), and a surface modification load of ∼40%. The *in vitro* stability of GNRs-PEG-TPEI was verified. The cellular imaging results demonstrated that the nanoprobe could efficiently recognize several types of tumor cells including MCF-7, HepG2, and Caco-2 while exhibiting specific fluorescence signals only after interacting with tumor cells and minimal background interference. In addition, the study investigated the toxicity of the nanoprobe to the captured cells and proved the safety of the nanoprobe. In conclusion, a specific and efficient nanoprobe was developed for capture and detection of different types of tumor cells based on their unique metabolic characteristics. It holds great promise for achieving early diagnosis and monitoring the tumor progression by detecting the CTCs in clinical liquid biopsy samples.

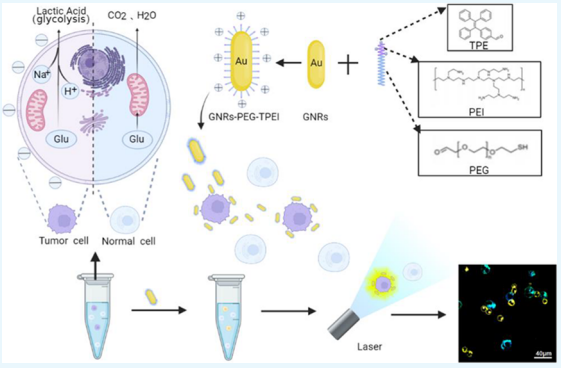

1. INTRODUCTION

Cancer is one of the leading causes of death worldwide, affecting millions of people each year.[1] The survival rates of cancer are closely related to the stage of the diseases being diagnosed. The lack of early detection strategies is responsible for the high death rates of cancer.[2−5] More than 90% of cancer deaths are caused by late-stage metastasis.[3] At present, most of the conventional tumor diagnosis methods have poor timeliness, failing to indicate the early-stage tumors.[4−6] Circulating tumor cells (CTCs) are tumor cells being released into the blood circulation or elsewhere as a result of spontaneous departure or metastasis from the original tumor sites.[6,7] CTCs could be early-stage and real-time biomarkers for the analysis of the biological characteristics of the tumor in liquid biopsy samples.[6,8,9] However, CTCs in peripheral blood, a common type of liquid biopsy, are too rare to be detected directly by routine analytical techniques.[10] It is essential to capture the CTCs from liquid biopsy samples before they are subjected to detailed detection. CTC capture methods could be divided into two categories: methods based on cellular immunological characteristics and methods based on physical characteristics of tumor cells.[11] Methods based on cellular immunological characteristics may provide false negative information due to the various surface characteristics of different types of CTCs or the heterogeneity of CTCs from the same origins, especially for early-stage tumor screening, when the types and immunological characteristics of CTCs are uncertain and could not be predicted.[12] It would be beneficial and crucial to establish a universal CTC detection method for most tumors. The enrichment method based on physical properties is mainly based on the physical properties of CTCs, such as the volume size, density, electrophoretic properties, cell rigidity, etc.[13,14] For example, the widely used microporous filtration method is used to capture CTCs based on the characteristics that the volume of CTCs is larger than blood cells and they do not easily deform.[14] In addition, there are density gradient centrifugation based on CTC density, dielectric electrophoresis (DEP) based on the CTC charge, etc.[15] These methods are simple because they generally do not require preprocessing of the patient's blood and do not rely on specific antigens. In

Received: March 16, 2022
Accepted: May 6, 2022
Published: May 17, 2022

Scheme 1. Schematic Diagram of a Positively Charged Fluorescence "Turn-On" Nanoprobe with GNRs as the Carrier, TPE as the Fluorescence Donor, and PEI as the Targeting Moieties for Recognizing Tumor Cells Based on Cellular Metabolic Properties, Providing Specific Fluorescence Signals after Binding with Tumor Cells

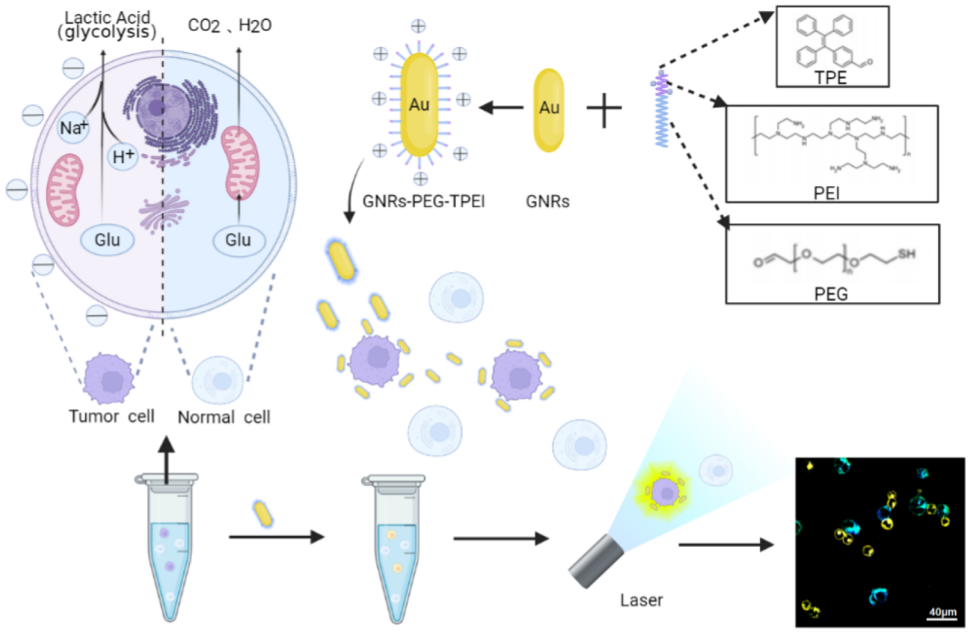

addition, the isolated cells can maintain integrated cell activity for downstream analysis. Because the physical properties of CTCs from different tumor sources and those with an epithelial−mesenchymal transition (EMT) remain relatively uniform, a physical property-based strategy has shown good performance in capturing these cells.[16] It is still worth mentioning that these methods inevitably have defects with poor specificity, such as the omission of smaller CTCs when enriching according to the size of CTCs can lead to deflection results from partially obtained CTCs.[14,17] Given the current status of CTC analysis in liquid biopsy, improved approaches for capture and detection of CTCs specifically and efficiently are still worth exploring.

Studies have found that cancer cells metabolize energy differently from normal cells.[18−20] By comparing the energy metabolism patterns, the glucose uptake and lactate secretion were found to be up to 30 times higher in tumor cells than those in normal cells, a phenomenon known as the Warburg effect.[18,20] Previous studies have shown that when a large quantity of lactate salts produced through aerobic glycolysis of tumor cells were transported out of the cells, they would take away cations such as H^+, K^+, and Na^+ on the cell surface, resulting in an imbalance of the cell surface charge and thus forming a much more negative charge network on the membrane of tumor cells.[21−24] In comparison, normal cells only produce a small amount of lactate salts during aerobic respiration.[25] Therefore, the strong surface negative charge network of tumor cells could serve as a broad spectrum covering most tumor cell types and efficient capture features. As a result, positively charged probes could specifically bind to tumor cells with relatively stronger electrostatic interactions. Researchers have studied the cell surface charge by observing the number of cells combined with different electrical nanomagnetic beads.[26] It was found that 22 different types of tumor cells, including common cervical cancer cells (HeLa cells), breast cancer cells (MCF-7 cells), prostate cancer cells (PC-3 cells), and ovarian adenocarcinoma cells (SKOV3 cells), had a stronger negative charge on the surface compared with normal cells.[24] Therefore, CTC detection characterized by metabolic abnormality could be a broad-spectrum target for most tumor cell types in the application of early-stage tumor screening. Design and development of metabolically targeted cationic probes are urgent needs for verifying the above findings and providing promising tools for CTC detection.

Nanotechnology is an ideal strategy for cell capture and detection and is widely used in the detection of biological samples with high sensitivity and specificity.[27−29] Nanomaterials have a relatively large surface area, enabling efficient interactions with the target for separation. Among various nanoplatforms, gold nanoparticles are easy to synthesize with extraordinary surface reactivity and biocompatibility, especially their excellent optical properties, which are perfect for the detection of biological samples.[30,31] The synthesis technology of gold nanoparticles is mature, and the size and shape of the product can be precisely controlled by adjusting the amount of the reaction reagent, yielding gold nanospheres, gold nanorods (GNRs),[32] gold nanoclusters, or gold nanocages.[33] Especially for gold nanorods, the anisotropic gold nanorods possess stronger local surface plasmon resonance (LSPR) properties.[34] The LSPR peak in the near-infrared region of GNRs has a unique role in background reduction during the detection and analysis of biological samples due to the optical absorption of the organism's spontaneous fluorescence in the range of 650−900 nm. In addition, the LSPR property can also significantly enhance the Raman signal of molecules adsorbed on the surface of GNRs,[35] known as surface-enhanced Raman scattering (SERS), providing more options for subsequent detection after capture. It should be noted that a bilayer of cationic surfactants would be readily formed on the surface of GNRs during classic preparation, which is a main source of cytotoxicity.[36−39] To reduce this cytotoxicity without affecting stability, GNRs are often modified with modifiers including polymers, polyelectrolytes, silica shells, and polysaccharides. Polyethylene glycol (PEG) is a polymer with excellent water

https://doi.org/10.1021/acsomega.2c01494
ACS Omega 2022, 7, 18073−18084

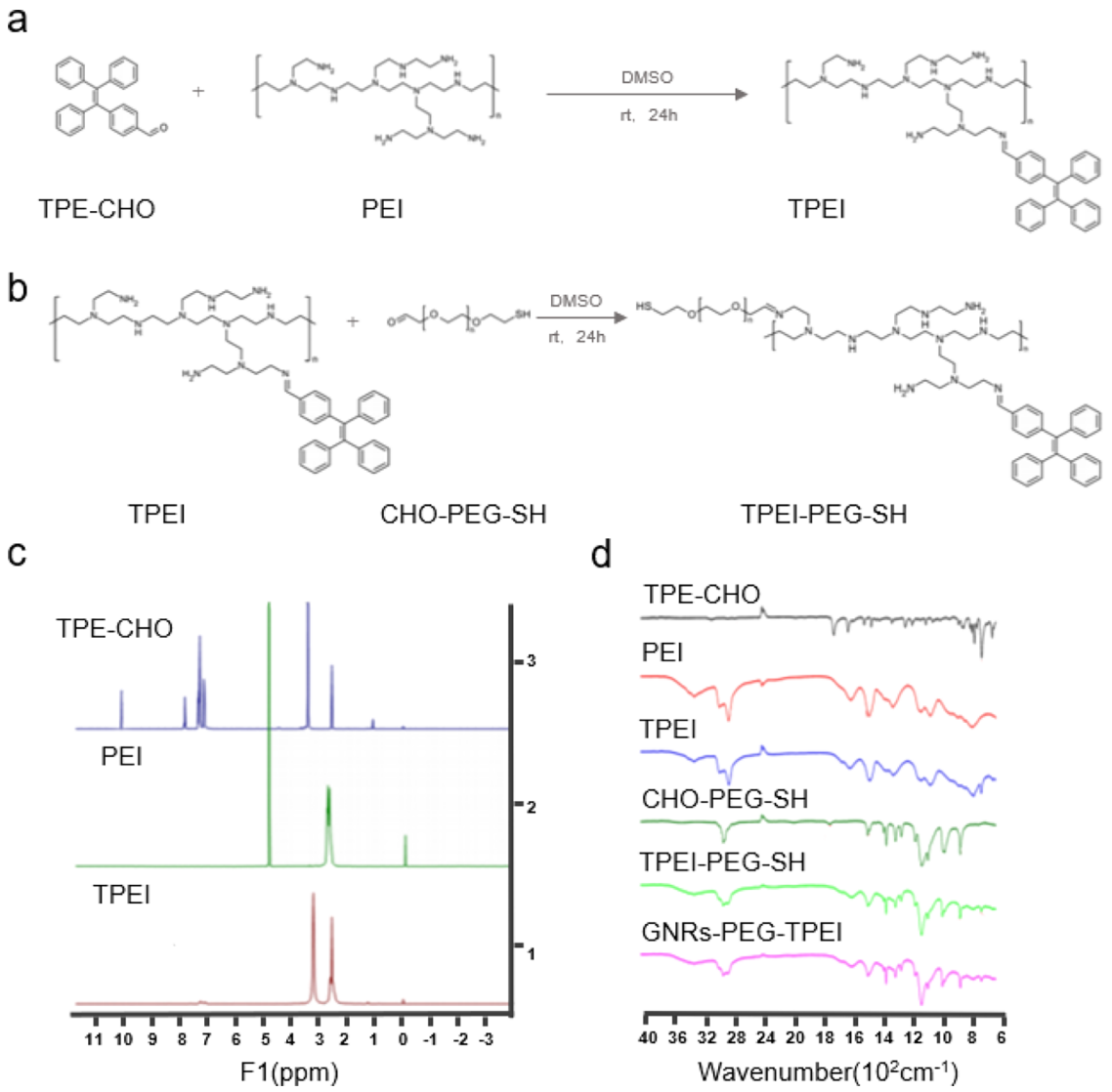

Figure 1. Synthesis and characterization of TPEI-PEG-SH. (a) Synthetic route for TPEI. (b) Synthetic route for TPEI-PEG-SH. (c) ^{1}H NMR spectra of TPE-CHO, PEI, and TPEI. (d) FT-IR spectra of TPE-CHO, PEI, TPEI, CHO-PEG-SH, TPEI-PEG-SH, and GNRs-PEG-TPEI.

solubility and biocompatibility.[40,41] As the thiol group (−SH) can form a stable Au−S bond with gold (Au), PEG can be effectively grafted to the surface of GNRs by terminal −SH modification.[42]

Fluorescence imaging has been widely used in biological imaging due to its advantages of high spatial resolution, good biocompatibility, low cost, and easy availability.[43] However, the traditional fluorescence molecules tend to aggregate in high concentrations of aqueous solution, leading to the fluorescence quenching due to $\pi-\pi$ stacking, which is called the aggregation-induced quenching (ACQ) effect.[44] Due to the ACQ phenomenon, traditional fluorescence dyes need to be applied in the form of low-concentration aqueous solution in biological detection systems, resulting in a relatively low fluorescence signal-to-noise ratio, poor photostability, low detection sensitivity, and poor stability.[45] With the discovery of the aggregation-induced emission (AIE) effect, AIE fluorescent molecules (named as AIEgens) present a new mode to complement the deficiency of ACQ.[46−48] Tetraphenylethene (TPE) is a classic AIEgen.[49] TPE is almost nonfluorescent in a free molecular state at a low-concentration solution. When it accumulates at a high-concentration solution or in a poor solvent, it would exhibit bright fluorescence.

To take advantage of GNRs and AIEgens for CTC detection, polyethylene imine (PEI), a cationic polymer, which can achieve specific targeted binding of the negative charge on the tumor cell surface as well as improve the water solubility of TPE, has been serving as a bridge for GNRs and AIEgens. On this basis, we have designed a positively charged, fluorescence "turn-on" nanoprobe with gold nanorods (GNRs) as the carrier, polyethylene imine (PEI) as the targeting moieties for recognizing tumor cells based on cellular metabolic properties, and the classical aggregation-induced emission (AIE) molecule tetraphenylethene (TPE) as the fluorescence "turn-on" indicator providing specific fluorescence signals after binding with tumor cells (Scheme 1). The positively charged polymer TPEI with an AIE effect was prepared by the Schiff base reaction between TPE and PEI. TPEI was further functionalized with a thiol group (−SH) through a bifunctional linker, yielding TPEI-PEG-SH. GNRs-PEG-TPEI was finally obtained by grafting TPEI-PEG-SH to the surface of GNRs *via* the ligand replacement principle.

https://doi.org/10.1021/acsomega.2c01494
ACS Omega 2022, 7, 18073−18084

In this study, the chemical characteristics and stability of GNRs-PEG-TPEI were investigated by multiple measurements including ^{1}H NMR (nuclear magnetic resonance), Fourier transform infrared (FT-IR) spectroscopy, and TEM (transmission electron microscopy). By the fluorescence imaging performance of GNRs-PEG-TPEI, the tumor-cell-targeted imaging specificity and sensitivity of the nanoprobe were evaluated. Finally, to investigate the cytotoxicity of GNRs-PEG-TPEI after tumor cell capture, cell membrane integrity, cell oxidative stress, and proto-oncogene expression were measured in this study.

2. RESULTS AND DISCUSSION

2.1. Characterization of TPEI-PEG-SH. To verify the successful synthesis of TPEI (TPE-PEI conjugates) through the TPE-CHO and PEI reaction (Figure 1a), the reactants and products were characterized by ^{1}H NMR (400 MHz) (Figure 1c). The H peak of the aldehyde group (−CHO) in the low-field region of the product disappeared with a new peak appearing at δ 8.21, which was presumed to be H around the newly formed imine bond. At the same time, the chemical shift of H from the TPE-CHO benzene ring in the new product moved to the high field, located at δ 7.47 (d, 2H), 7.11−6.97 (m, 11H), 6.95−6.91 (m, 6H). The above results showed that TPE-CHO reacted with PEI through the Schiff base reaction. Small molecular TPE was successfully modified on a macromolecular PEI chain, obtaining the target product TPEI.

Fourier transform infrared spectroscopy (FT-IR) was used to characterize the reaction product of TPEI and TPEI-PEG-SH (Figure 1d). The −CHO signal peak of TPE-CHO (1695.43 cm^{-1}) disappeared in the spectrum of TPEI, indicating that TPE-CHO was successfully conjugated to PEI, which was consistent with ^{1}H NMR results. The characteristic peaks from TPEI and CHO-PEG-SH can be seen in the spectra of TPEI-PEG-SH, which proved the successful synthesis of TPEI-PEG-SH (Figure 1b).

2.2. Characterization of GNRs-PEG-TPEI. The LSPR peaks of GNRs, GNRs-PEG, and GNRs-PEG-TPEI were characterized by UV−vis absorption spectra (Figure 2a). The transverse LSPR peak of GNRs was at 520 nm, while the longitudinal LSPR peak was at 730 nm. The UV−vis spectra of the product (GNRs-PEG-TPEI) did not change before and after CHO-PEG-SH or TPEI-PEG-SH modification. Compared with unmodified GNRs, the longitudinal LSPR peak positions of modified GNRs-PEG and GNRs-PEG-TPEI showed redshifts of 14 and 16 nm, respectively. This change was caused by the coupling groups on the surface of GNRs, indicating the successful modification of CHO-PEG-SH and TPEI-PEG-SH on the surface of GNRs.

The DLS particle size of the samples was measured by a Brookhaven Zetasizer (Figure 2b). The results showed that the average particle size of GNRs was 54.32 nm with a PDI of 0.188. The average particle size of GNRs-PEG was 126.21 nm (PDI = 0.140). For GNRs-PEG-TPEI, the average particle size was 171.87 nm (PDI = 0.268). The particle size results of DLS showed that the particle size increased as the molecular weights of the modified polymers on the surface of GNRs increased.

Zeta potential results showed that unmodified GNRs showed a strong positive charge (+42.42 mV) (Figure 2c). Unmodified GNRs are not suitable for living biological samples, such as cell testing, because of the cytotoxicity of CTAB.[36] The thiol group of PEG-SH could bind to GNR surface sites more stably in the form of the Au−S covalent bond while replacing CTAB. The surface charge of GNRs-PEG (+6.39 mV) was significantly weakened compared with that of GNRs due to the addition of PEG. As PEI is a positively charged polymer, the surface charge of GNRs-PEG-TPEI after TPEI-PEG-SH modification increased again, reaching +54.87 mV.

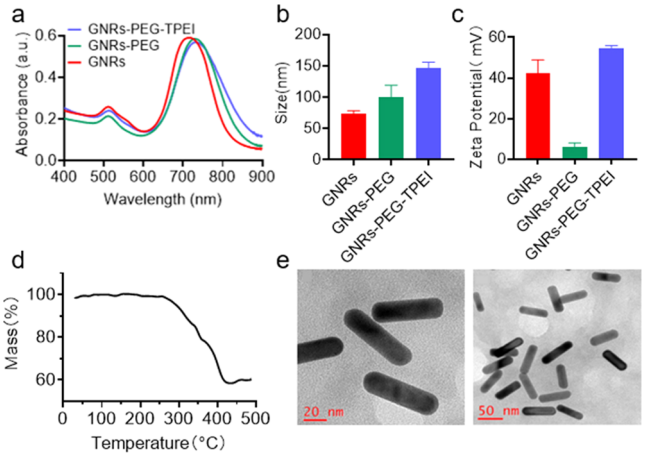

Figure 2. Characterization of GNRs-PEG-TPEI. (a) UV−vis absorption spectra of GNRs, GNRs-PEG, and GNRs-PEG-TPEI. (b) Particle sizes of GNRs, GNRs-PEG, and GNRs-PEG-TPEI. (c) Zeta potentials of GNRs, GNRs-PEG, and GNRs-PEG-TPEI. (d) Thermogravimetric curve of GNRs-PEG-TPEI. (e) Morphologies of GNRs-PEG-TPEI *via* TEM. Scale bar for the left image = 20 nm. Scale bar for the right image = 50 nm.

TGA analysis was used to test the actual load efficiency and thermal stability of TPEI-PEG-SH on GNR carriers (Figure 2d). According to the thermogravimetric curve, GNRs-PEG-TPEI experienced an obvious weight loss process when the temperature increased to 250 °C as TPEI-PEG-SH is an organic material and decomposes at high temperatures. By calculating the amount of weight loss, it could be estimated that the actual load of TPEI-PEG-SH on the surface of GNRs was about 40%.

To characterize the morphology of GNRs-PEG-TPEI, TEM imaging was carried out. As shown in Figure 2e, the nanoprobe GNRs-PEG-TPEI was in a regular rod shape, uniform, and well-dispersed with no agglomeration in the solution. The particle size of GNRs-PEG-TPEI was measured to be 65 nm in length and 18 nm in width, with an aspect ratio of 3.44:0.14 from TEM images.

2.3. Tumor Cell Targeting of GNRs-PEG-TPEI. The lactate secretion of tumor cells MCF-7, HepG2, and Caco-2 and normal cells NCM460 under normal culture conditions was initially investigated. The results showed that the lactate secretion of the three tumor cells was significantly higher than that of normal cells over a period of 24 h. Therefore, these four cells can be used as cell models to explore the targeting ability of GNRs-PEG-TPEI in subsequent experiments (Figure 3a). To obtain a tumor cell model with inhibition of lactate secretion, the effects of 3-bromopyruvic acid (3-BP), a direct inhibitor of glycolysis, and dichloroacetic acid (DCA), an indirect inhibitor, were investigated. 3-BP could inhibit the lactate secretion of tumor cells at a concentration of 50 μM. When the concentration reached 200 μM, the lactate secretion of tumor cells decreased to 10−40% (Figure 3b), while DCA showed strong lactate secretion inhibition from 10 to 40 mM

https://doi.org/10.1021/acsomega.2c01494
ACS Omega 2022, 7, 18073−18084

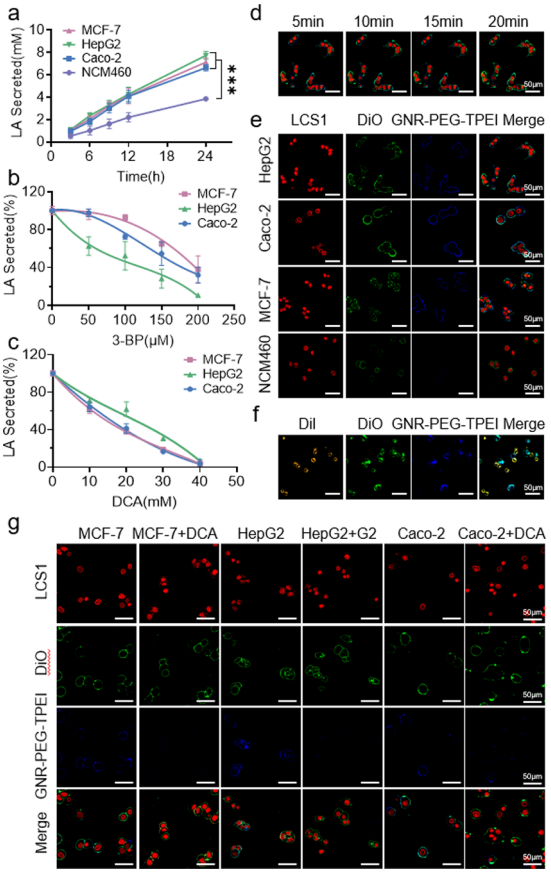

Figure 3. Mechanism of targeting abilities. (a) LA secretion of cells under normal culture conditions (***$p < 0.001$). (b) Effects of glycolysis inhibitors 3-BP on LA secretion. (c) Effects of glycolysis inhibitors DCA on LA secretion. (d) Fluorescence images of MCF-7 and GNRs-PEG-TPEI incubated for different times (red: Nuclear Red LCS1 dyes the nucleus, green: DiO dyes the membrane, and blue: GNRs-PEG-TPEI dyes the negatively charged cell membrane). (e) Fluorescence images of GNRs-PEG-TPEI applied to HepG2, Caco-2, MCF-7, and NCM460 (red: Nuclear Red LCS1 dyes the nucleus, green: DiO dyes the membrane, and blue: GNRs-PEG-TPEI dyes the negatively charged cell membrane). (f) Fluorescence images of GNRs-PEG-TPEI applied to coculture of Caco-2 and NCM460 (orange-red: DiI dyes the membrane of NCM460, green: DiO dyes the membrane of Caco-2, and blue: GNRs-PEG-TPEI dyes the negatively charged cell membrane). (g) Effect of DCA on cell fluorescence imaging (red: Nuclear Red LCS1 dyes the nucleus, green: DiO dyes the membrane, and blue: GNRs-PEG-TPEI dyes the negatively charged cell membrane). Images were collected using a Plan-apochromat 63×/1.4 oil immersion objective by sequential scanning, with excitation at 405 and 488 nm. Emission was collected by photomultiplier tubes in the ranges of 423−492 and 590−700 nm, respectively.

(Figure 3c). In conclusion, the inhibitory concentration of the indirect inhibitor DCA was 200 times larger than that of 3-BP, indicating that 3-BP had stronger inhibitory activity. However, the inhibitory performance of DCA among the three tumor cells was more stable, while the inhibitory effect of 3-BP was greatly different among different cells. Therefore, in subsequent experiments, DCA with a concentration of 30 mM was selected to obtain tumor cell models with decreased lactate secretion.

Figure 3d shows the confocal imaging results of MCF-7 cells incubated with GNRs-PEG-TPEI, in which the red signal indicates the cell nucleus, the green signal indicates the cell membrane, and the blue signal represents GNRs-PEG-TPEI. The blue signal and the green signal were colocalized, indicating that GNRs-PEG-TPEI was mainly trapped on the cell membrane after 5 min of incubation with tumor cells. When cells were observed after 20 min of incubation, the nanoprobe signal was still colocalized with cell membrane staining, indicating that endocytosis of GNRs-PEG-TPEI did not occur during this period. Based on the above results, it was clear that (1) the metabolically based negative-charge-targeted nanoprobe could achieve instant tumor cell imaging. The specific fluorescence signal appeared in as short as 5 min once the nanoprobe bonded to the tumor cell membrane through the electrostatic interaction. Compared with conventional antigen−antibody recognition, which may take several hours, the nanoprobe designed in this study could be used for rapid tumor cell detection; (2) GNRs-PEG-TPEI did not go through rapid endocytosis within at least 20 min, which was beneficial to maintaining cell activity and stability of genetic information while reducing the interference to downstream biological analysis after tumor cell capture by the nanoprobe; (3) bright fluorescence was detected after GNRs-PEG-TPEI binding to the MCF-7 cell membrane. Meanwhile, free GNRs-PEG-TPEI only exhibited a minimal background signal, indicating that GNRs-PEG-TPEI was a fluorescence "turn-on" probe by taking advantage of the AIE effect. It provided a more convenient detection process omitting the removal of free probes, thus reducing the positive cell loss during washing and the risk of false negative results.

Fluorescence imaging results of GNRs-PEG-TPEI incubation with tumor cells or normal cells showed that the cell membranes showed a bright fluorescence signal when GNRs-PEG-TPEI was bound to MCF-7, HepG2, and Caco-2, indicating the robustness of the nanoprobe to recognize a variety of tumor cells. However, under the same operation process and shooting parameters, only a weak fluorescence signal was detected on the cell membrane of normal cells NCM460, indicating that the nanoprobe could target tumor cells exhibiting a strong fluorescence signal and could rarely bind to normal cells with only minimal background noise (Figure 3e).

For further evaluating the targeting specificity of GNRs-PEG-TPEI between tumor cells and normal cells, GNRs-PEG-TPEI was incubated with cocultured Caco-2 and NCM460. AIE fluorescence was observed on the cell surface. The cell membrane of NCM460 was labeled with an orange-red DiI dye, while the Caco-2 cell membrane was labeled with a green DiO dye. As shown in Figure 3f, the AIE fluorescence signal of GNRs-PEG-TPEI was colocalized with green fluorescence (Caco-2 cell membrane). The AIE fluorescence from the NCM460 cell membrane was significantly weaker than that from the Caco-2 cell membrane, indicating that much fewer GNRs-PEG-TPEI nanoprobes aggregated on the surface of the normal cell membrane. It was reasonable as normal cells mainly adopted the respiration mode of the tricarboxylic acid cycle, which did not produce a large amount of lactic acid with only a weak negative charge on the cell membrane surface. This result indicated that the nanoprobe could distinguish tumor cells from normal cells, showing the feasibility for the application of CTC detection in liquid biopsy samples in the future.

To test the targeting intensity of the nanoprobe, tumor cells with different levels of lactic acid secretion, modeled by the use

https://doi.org/10.1021/acsomega.2c01494
ACS Omega 2022, 7, 18073−18084

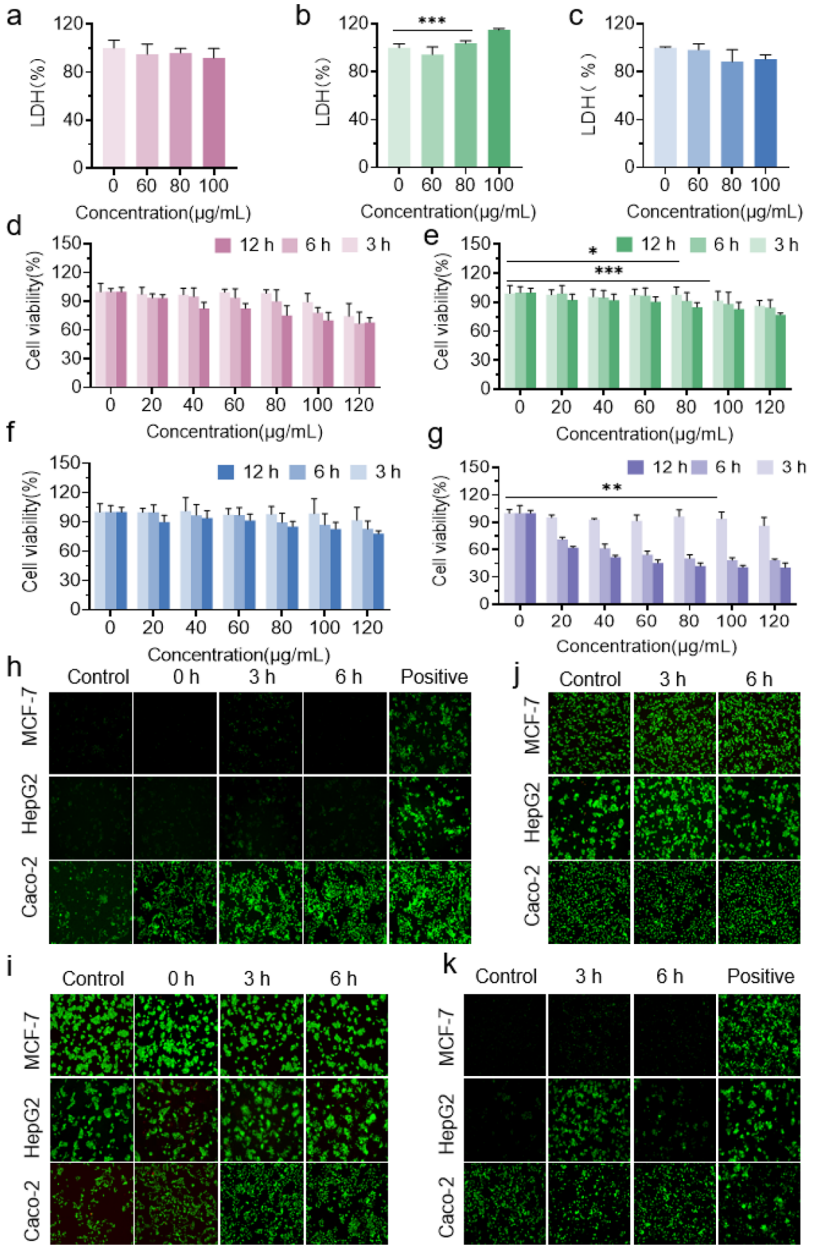

Figure 4. Cytotoxicity test. LDH release of cells treated with GNRs-PEG-TPEI at different concentrations: (a) MCF-7, (b) HepG2 (***$p < 0.001$ for 0 μg/mL *vs* 100 μg/mL), and (c) Caco-2. Cell viabilities of GNRs-PEG-TPEI at different concentrations: (d) MCF-7, (e) HepG2 (*$p < 0.05$ for 0 μg/mL *vs* 100 μg/mL (3 h) and ***$p < 0.001$ for 0 μg/mL *vs* 120 μg/mL (3 h)), (f) Caco-2, and (g) NCM460 (**$p < 0.01$ for 0 μg/mL *vs* 120 μg/mL (3 h)). (h) ROS productions of adherent cells captured by GNRs-PEG-TPEI and reculture. (i) ROS productions of suspension cells captured by GNRs-PEG-TPEI and reculture. (j) Survival conditions of adherent cells captured by GNRs-PEG-TPEI and reculture. (k) Survival conditions of suspension cells captured by GNRs-PEG-TPEI and reculture (green: LiveDye dyes living cells and red: NucleiDye dyes dead cells).

of the glycolysis inhibitor DCA, were imaged with the nanoprobe under the same operating process and shooting parameters. As shown in Figure 3g, the fluorescence intensity from the tumor cell membrane without DCA treatment was generally stronger than that of DCA-treated tumor cells, indicating that the targeting and fluorescence "turn-on" efficiency of GNRs-PEG-TPEI were positively correlated with the level of lactate secretion by cells. The nanoprobe could selectively bind to cells with a higher aerobic glycolysis level.

2.4. Potential of GNRs-PEG-TPEI Nanoprobes for Tumor Detection. In addition, a Raman detection system was tested for exploring the potential of downstream analysis of tumor cells after GNRs-PEG-TPEI nanoprobe capture. Basically, GNRs-PEG-TPEI was labeled with the Raman-active molecule 4-ATP. The SERS signal of single cells was obtained after nanoprobe incubation. As shown in Figure S1, GNRs-PEG-TPEI/4-ATP could bind with tumor cells with a stronger surface negative charge. In addition to AIE-induced "turn-on" fluorescence, the aggregation of GNRs-PEG-TPEI/4-ATP resulted in an increase in the concentration of 4-ATP at the detection sites generating the SERS active sites. The SERS signal of 4-ATP was significantly enhanced by the electromagnetic field enhancement effect. Single tumor cells were successfully detected by SERS. These results indicated that GNRs-PEG-TPEI nanoprobe detection was compatible with

https://doi.org/10.1021/acsomega.2c01494
ACS Omega 2022, 7, 18073−18084

subsequent biological analysis after specific tumor cell capture such as Raman imaging analysis, which paved the way for identifying detailed CTC information following nanoprobe capture for early diagnosis and tumor heterogeneity studies in the future.

2.5. Cytotoxicity Evaluation of GNRs-PEG-TPEI. Considering the positive charge on the surface of GNRs-PEG-TPEI, the integrity of the cell membrane may be damaged when the nanoprobe interacted with cells, leading to cell apoptosis or necrosis. Once the cell membrane was damaged, LDH would be released into the medium from cells.[50,51] LDH is often used as an indicator to measure the integrity of the cell membrane. As shown in Figure 4a−c, GNRs-PEG-TPEI rarely induced cell membrane damage at concentrations of 60−100 μg/mL after 3 h of incubation with cells except that slight LDH leakage was observed in HepG2 cells with a nanoprobe concentration of 100 μg/mL, which is 25% higher than the nanoprobe working concentration. Overall, the results indicated that the nanoprobe exerted little effect on cell membrane integrity.

According to the cell viability results shown in Figure 4d−g, when GNRs-PEG-TPEI was incubated with cells for 3 h within the range of applied concentrations, the nanoprobe had no significant cytotoxicity to all four types of cells.

The level of cellular oxidative stress induced by GNRs-PEG-TPEI could be assessed by measuring intracellular ROS production.[52] For the positive control group, the cellular ROS level would be elevated after the cells were stimulated by the positive control solution in the ROS fluorescence kit. In Figure 4h,i, the intensity of green fluorescence was positively correlated with the amount of ROS production. As shown in Figure 4h, for different tumor cells, the cellular ROS production of the nanoprobe-captured and recultured cells showed different trends as the culture time increased. No significant ROS production was observed in MCF-7 and HepG2 cells within 6 h after nanoprobe capture and reculture. Meanwhile, a large amount of ROS production could be seen in Caco-2 cells at 0 h. In addition, the ROS level continued to increase from 3 to 6 h after reculture, indicating that Caco-2 cells were more sensitive to GNRs-PEG-TPEI and prone to cellular oxidative stress during the capture process. As shown in Figure 4i, the ROS production trends of GNRs-PEG-TPEI-incubated suspension cells after capture and reculture were roughly the same as those with adherent cells. ROS production was not obvious in MCF-7 cells within 6 h. HepG2 cells produced a small amount of ROS at 3 h, and the ROS level decreased at 6 h, indicating that HepG2 cells could spontaneously reduce oxidative stress through a redox balance, meaning that ROS damage caused to cells by capture might be recoverable. It should be mentioned that the control group in which Caco-2 cells were only subjected to repeated centrifugation without GNRs-PEG-TPEI incubation also produced a certain amount of ROS, indicating that the cells were more sensitive to experimental operations and prone to oxidative stress.

LIVE/DEAD staining results of the cells going through capture and reculture were observed by fluorescence microscopy. The green fluorescence signal (Figure 4j) and the red fluorescence signal (Figure 4k) indicated living cells and dead cells, respectively. After comparing the ratio of the green signal to the red signal, it could be concluded that the number of living cells of both adherent cells and suspended cells after capture and reculture was significantly more than that of dead cells. The cell viability was preserved after nanoprobe capture and reculture processes.

2.6. Genotoxicity Evaluation of GNRs-PEG-TPEI. The mRNA expression levels of proto-oncogenes in MCF-7, HepG2, and Caco-2 after GNRs-PEG-TPEI capture and reculture were detected by real-time RT-PCR to explore the genotoxicity of the nanoprobe to cells. The three highly expressed proto-oncogenes in tumor cells were the *ras* gene, *c-fos*, and *c-myc* among which *c-myc* and *N-ras* played a synergistic role in tumor genesis. The mRNA expression of each cell measured by real-time fluorescence quantitative PCR is shown in Figure S2. The results showed that compared with suspension cells, the proto-oncogene mRNA expression levels of adherent cells were generally significantly changed after GNRs-PEG-TPEI capture and reculture. Compared with adherent cells, probes of suspended cells release cells more completely. The results showed that the probe had little effect on gene expression as long as the probe was released completely after capture.

3. CONCLUSIONS

CTC detection holds great promise for early diagnosis of tumors or monitoring the tumor progression and prognosis after treatment. It is crucial to capture and detect these cells precisely since their abundance is pretty low in liquid biopsy samples. Ideal CTC detection methods should, on the one hand, recognize tumor cells from other normal cells specifically and, on the other hand, recognize tumor cells broadly regardless of their specific types as for early diagnosis since the types of tumor cells are unknown until they are further identified. Based on the difference of energy metabolic pathways, the surface negative charge of tumor cells is much stronger than that of normal cells because of the excessive lactic acid production by aerobic glycolysis of tumor cells. As a result, the cationic polymer PEI was modified to GNRs for targeting tumor cells in this study. As a detection nanoprobe, to further improve the sensitivity and reduce the false negative results, an AIE dye (TPE) was also built into the nanoprobe, which would start the fluorescence "turn-on" mode when more nanoprobes aggregated on the surface of tumor cells because of stronger electrostatic interactions. In this study, we successfully prepared nanoprobes with a uniform morphology and specific recognition of tumor cells. The study proved that the nanoprobe would not produce toxicity to the captured cells, and more accurate downstream analysis could be carried out, such as single cell imaging through SERS. Based on the preliminary results of this study, we will continue to optimize the probe system in the follow-up to verify the capture ability of CTCs in liquid samples in clinical practice and explore the combination of precise downstream analysis methods for promoting the application to clinical application.

4. EXPERIMENTAL SECTION

4.1. Materials and Reagents. Cetyltrimethylammonium bromide (CTAB, 99%) was purchased from Aladdin (Shanghai, China). Dichloroacetic acid (DCA, GR, 99%), 4-aminothiophenol (4-ATP, 97%), 3-bromopyruvic acid (3-BP, >95%), and doxorubicin (DOX, >98%) were purchased from Macklin (Shanghai, China). Silver nitrate ($AgNO_3$, >99%) was purchased from Alfa Aesar (Shanghai, China). Sodium borohydride (NaBH4, 98%) was purchased from Ino kay (Beijing, China). 4-(1,2,2-Triphenylvinyl)benzaldehyde (TPE-

https://doi.org/10.1021/acsomega.2c01494
ACS Omega 2022, 7, 18073−18084

CHO, 97%) was purchased from Alpha (Zhengzhou, China). Aldehyde−polyethylene glycol−sulfhydryl group (CHO-PEG-SH, M_W = 2000 Da, AR) was purchased from Ruixi (Xi'an, China). Dimethyl sulfoxide (DMSO, AR), isopropanol (AR), and ethanol (AR) were purchased from Zhiyuan (Tianjin, China). L-Ascorbic acid (vitamin C, AR), hydrochloric acid (HCl, GR), and chloroform (AR) were purchased from Chemical Reagent (Guangzhou, China). Basic DMEM, high-glucose (4.5 g/L), penicillin−streptomycin (5000 U/mL), fetal bovine serum (FBS), and trypsin−EDTA (0.25%) were purchased from Gibco (New York, America). The cell membrane dye DiO (maximum wavelengths of excitation/emission of 484/501 nm), DiI (maximum wavelengths of excitation/emission of 549/565 nm), Nuclear Red LCS1 AAT, and RNase-free water were purchased from Beyotime (Shanghai, China). Thiazole bromide blue tetrazolium (MTT) and lactate dehydrogenase colorimetric assay kits were purchased from Solarbio (Beijing, China). An L-lactic acid colorimetric assay kit and a reactive oxygen species colorimetric assay kit were purchased from Elabscience (Wuhan, China). A live and dead cell double staining kit was purchased from Abbkine (America). A TRIzol reagent was purchased from Life Invitrogen (America). A ReverTra Ace qPCR RT master mix with a gDNA remover and a SYBRGreen real-time PCR master mix were purchased from Toyobol (Shanghai, China). A phosphate buffer system (PBS, pH 7.0−7.2) was purchased from HyClone (America). All primers (sequences are shown in Table S1) were synthesized and purified by Sangon Biotech (Shanghai, China).

4.2. Apparatus. The hydrogen spectrum (^{1}H NMR) was characterized by a 400 MHz nuclear magnetic resonance spectrometer (NMR, AvanceIII, Bruker, Germany) at room temperature to confirm the chemical structure. A Fourier transform infrared spectrometer (FT-IR, IRAffinity-1S, Shimadzu, Japan) was used for infrared characterization of the samples. UV−vis spectra were measured on a UV−vis spectrometer (UV-2600, Shimadzu, Japan). The particle size and the zeta potential were measured at 25 °C on a Brookhaven Zetasizer NanoZS instrument (90Plus PALS, America). The morphology of the materials was observed with a transmission electron microscope (TEM, JEM2100, JEOL, Japan). Thermogravimetric analysis (TGA) results by a simultaneous thermal analyzer (STA, 409PC, Netzsch, Germany) were used to analyze the surface modification load of the nanoprobe. Confocal laser microscopy images were captured by a confocal laser scanning microscope (CLSM, LSM880, Zeiss, Germany). A laser confocal Raman spectrometer (Renishaw inVia, Renishaw, England) was used to detect the SERS spectra of samples. An MTT assay was performed with a multimode reader (Epoch2, BioTek, America). In order to explore the gene toxicity of GNRs-PEG-TPEI to cells, the mRNA expression of each cell was measured in real time by real-time quantitative PCR (QuantStudio 3, ABI, America).

4.3. Cell Lines and Culture Conditions. Cell lines used in this study were obtained from the Chinese Academy of Sciences Cell Bank (Shanghai, China). MCF-7 cells (human breast cancer cells), HepG2 cells (human hepatocellular cancer cells), Caco-2 (human colorectal cancer cells), and NCM460 (human colonic epithelial cells) were cultured in complete Dulbecco's modified Eagle's medium (DMEM (4.5 g/L)) supplemented with 10% fetal bovine serum (FBS) and 1% penicillin−streptomycin. All the cells were maintained under a humidified atmosphere containing 5% CO_2 at 37 °C. Depending on the purpose of the experiment, the cells were seeded on 6-well plates, 24-well plates, 96-well plates, confocal dishes, or 25 cm^2 flasks. All sterile plastics were sourced from Corning (New York, America).

4.4. Synthesis of TPEI-PEG-SH. TPEI-PEG-SH was synthesized through two steps of the Schiff base reaction between the aldehyde group (−CHO) and the amine group ($-NH_2$), according to the method described previously.[53] Briefly, TPE-CHO (20 mg) and PEI (240 mg) were mixed in 5 mL of DMSO and stirred for 24 h at room temperature to obtain the conjugates (TPE-PEI) named as TPEI. The mixture was dialyzed (dialysis membrane molecular weight cutoff (MWCO) of 2 kDa) against deionized water for 24 h to remove DMSO. Then, the lyophilized TPEI (32 mg) and CHO-PEG-SH (32 mg) were dissolved in 5 mL of deionized water and stirred for 24 h at room temperature. The solution of TPEI-PEG-SH was finally lyophilized to get dried products.

The chemical structure of TPEI was confirmed with a 400 MHz NMR spectrometer, using tetramethylsilane as an internal standard. Fourier transform infrared (FT-IR) spectroscopy measurements were recorded to confirm the successful synthesis of TPEI-PEG-SH.

4.5. Preparation of GNRs-PEG-TPEI. CTAB-coated GNRs (GNR-CTAB) were synthesized by a seed-mediated growth method, with minor revisions.[38,39] Briefly, 0.1 mL of 20 mM $HAuCl_4$ was mixed with 8 mL of 0.1 M CTAB solution. Then, 0.48 mL of fresh ice-cold 0.01 M $NaBH_4$ was added under vigorous oscillation. The oscillation was stopped after 2 min. After 2 h of standing at room temperature, the brown-yellow solution was further used as the seed solution. The growth solution was prepared by mixing 1 mL of 20 mM $HAuCl_4$, 40 mL of 0.1 M CTAB, 400 μL of 10 mM $AgNO_3$, 220 μL of 0.1 MAA, and 160 μL of 1 M HCl solution together. Then, 48 μL of seed solution was added to the growth solution. The mixture was homogenized by shaking gently for 30 s and left undisturbed overnight to obtain GNRs.

For further surface modification, the as-prepared solution of GNRs (40 mL) was centrifuged twice at 12,000 rpm for 15 min to remove excess CTAB. The purified GNRs were redispersed in 40 mL of deionized water. Then, 5 mL of TPEI-PEG-SH (12.8 mg/mL) water solution was added slowly into 40 mL of the purified GNRs in deionized water and stirred for 16 h at room temperature. The mixed solution was continued to be dialyzed with deionized water for 24 h (dialysis membrane MWCO of 8−14 kDa). CTAB was gradually separated from the reaction system, which prompted more TPEI-PEG-SH to bind to the surface of GNRs. Finally, GNRs-PEG-TPEI was purified by repeated centrifugation and redispersed in deionized water for further use. GNRs-PEG was obtained with the same method by using CHO-PEG-SH. The sizes and zeta potentials of the GNRs, GNRs-PEG, and GNRs-PEG-TPEI were determined using dynamic light scattering (DLS). The morphology was studied using transmission electron microscopy (TEM). The UV−vis spectra of GNRs, GNRs-PEG, and GNRs-PEG-TPEI were measured from 400 to 900 nm.

4.6. Tumor Cell Targeting Mechanism Based on Metabolic Abnormality. Since the targeting mechanism of the positively charged nanoprobe GNRs-PEG-TPEI was based on the findings that tumor cells actively secreted a large quantity of lactic acid by aerobic glycolysis, this study first investigated the lactic acid secretion differences between tumor

https://doi.org/10.1021/acsomega.2c01494
ACS Omega 2022, 7, 18073−18084

cells and normal cells and the factors that affected lactic acid secretion. They were crucial to determining the experimental cell lines and the modeling conditions for inhibiting the secretion of lactic acid. Second, GNRs-PEG-TPEI was incubated with normal cultured cell lines and cell lines with reduced lactate secretion through modeling at room temperature to observe the fluorescence signal of the nanoprobe and determine whether GNRs-PEG-TPEI exhibited targeting recognition to tumor cells with high lactate secretion by measuring the fluorescence intensity.

The lactate secretion ability of the four cell lines mentioned above was investigated. Since the residual lactic acid in FBS would affect the results, the complete medium was discarded when each cell line grew to 80% confluence. Instead, 8 mL of DMEM high-glucose serum-free culture medium containing 1% penicillin−streptomycin was carefully added. One hundred microliters of medium was taken at 3, 6, 9, 12, and 24 h, with a 100 μL fresh medium supplement. The cell culture medium supernatant was collected at 10,000 rpm at 4 °C for 10 min with a centrifuge and stored at −20 °C for later use. The lactic acid concentration of the cell supernatant can be measured with a colorimetric kit of L-lactic acid (LA). To further clarify the targeting mechanism of the designed gold nanoprobe, DCA was used to inhibit the secretion of lactic acid. DCA is an indirect inhibitor of glycolysis, which does not directly inhibit any enzyme of the glycolysis pathway. Rather, it promotes oxidation of pyruvate in mitochondria and in turn shunts the pyruvate away from becoming lactate, thus inhibiting the conversion of pyruvate to lactate. The cells were grown under normal culture conditions to 30% confluency. Various concentrations of DCA were added to cell culture medium and incubated at 37 °C for 48 h. The binding of GNRs-PEG-TPEI to cells was observed by laser confocal fluorescence microscopy.

4.7. Tumor Cell Targeting of GNRs-PEG-TPEI. To investigate the ability of targeted binding between nanoprobes and tumor cells by fluorescence imaging, GNRs-PEG-TPEI in PBS was applied to the prepared cell samples at working concentrations making the final concentration of GNRs-PEG-TPEI 80 μg/mL. Cell nuclei were stained with Nuclear Red LCS1 (maximum wavelengths of excitation/emission of 622/645 nm). The cell membrane was stained with either a DiO dye (maximum wavelengths of excitation/emission of 484/501 nm) or a DiI dye (maximum wavelengths of excitation/emission of 549/565 nm). Without washing the free nanoprobes, fluorescence images were directly captured by a laser confocal microscope to observe the fluorescence signals of GNRs-PEG-TPEI.

4.8. Raman Measurements. As a kind of Raman-active molecule, 4-aminothiophenol (4-ATP) can label GNRs-PEG-TPEI and detect SERS signals on the cell surface. First, GNRs-PEG-TPEI/4-ATP was constructed. One hundred microliters of 4-ATP solution (10 μmol/L) was added into 10 mL of GNRs-PEG-TPEI solution (1 mg/mL), mixed evenly, and stirred for 30 min at room temperature. The products were processed with double steam water for 24 h (with a molecular weight of 8000 Da trapped) and continuously stirred. The water was changed every 6 h until the end of dialysis. The original solution was centrifuged at 8000 rpm for 5 min. Then, after the supernatant was discarded, precipitation was suspended by double distilled water to obtain GNRs-PEG-TPEI/4-ATP solution. Then, GNRs-PEG-TPEI cell SERS detection was performed. After digestion with trypsin, the cell density reached 1×10^6/mL by resuscitation with PBS. GNRs-PEG-TPEI/4-ATP solution was added into the cell suspension to make the concentration of GNRs-PEG-TPEI/4-ATP 80 μg/mL, and the cells were cultured for 5 min. The samples to be tested were dropped on quartz glass slides, and the SERS spectra of the samples were detected by a confocal micro-Raman spectrometer. SERS signals of tumor cells MCF-7, HepG2, Caco-2 and normal cells NCM460 were collected under 785 nm excitation light.

4.9. Cytotoxicity of GNRs-PEG-TPEI. For the cytotoxicity evaluation of the nanoprobes, cells were cultured in a 96-well plate and incubated with GNRs-PEG-TPEI with different concentrations at 37 °C for 3, 6, and 12 h. The MTT assay was utilized to evaluate the cytotoxicity of these materials. In brief, cells were incubated with culture medium containing 20 μL of MTT (5 mg/mL). After treatment for 4 h, the supernatant was discarded. Then, 100 μL of DMSO was added to dissolve the precipitates. The absorbance assay was measured at a wavelength of 490 nm in a microplate reader. The cell viability of treated groups was presented as the percentage of the adjusted absorbance with the untreated control groups.

Lactate dehydrogenase (LDH) release was also used to evaluate the cytotoxicity of the materials by an LDH release assay kit. When adherent cells grew to a confluence degree of 80%, GNRs-PEG-TPEI was added into DMEM high-glucose serum-free medium, and the final concentrations of GNRs-PEG-TPEI were 60, 80, and 100 μg/mL. After incubation for 3 h, the cell culture medium supernatant was collected at 10,000 rpm at 4 °C for 10 min with a centrifuge. Ten microliters of the sample was taken and placed in a 96-well plate. The lactate dehydrogenase concentration of the cell supernatant can be measured with a colorimetric kit of LDH.

$$\text{relative LDH release} = \frac{\Delta A_{450}\ (\text{drug})}{\Delta A_{450}\ (\text{control})} \times 100\%$$

where

$$\Delta A_{450}\ (\text{drug}) = A_{450}\ (\text{drug}) - A_{450}\ (\text{blank})$$

$$\Delta A_{450}\ (\text{control}) = A_{450}\ (\text{control}) - A_{450}\ (\text{blank})$$

4.10. Cell Viability after Nanoprobe Capture. Cell capture and reculture were simulated by both adherent cells and suspension cells. When adherent cells grew to a confluence degree of 80%, the supernatant was removed. DMEM medium containing 80 μg/mL GNRs-PEG-TPEI was added followed by incubation at room temperature for 20 min and solution removal. The cell surface was carefully washed with PBS three times. Complete medium was added and incubated at 37 °C for further culture. For suspension cells, DMEM medium containing 80 μg/mL GNRs-PEG-TPEI was added in an appropriate volume to make the cell density 1×10^6/mL. The cells were incubated at room temperature for 20 min and shaken every 5 min. After being centrifuged at 1000 rpm for 3 min, the supernatant was removed, and the cells were resuspended by adding the complete medium preheated at 37 °C. This was repeated twice. Finally, the cells were seeded in 12-well plates and incubated at 37 °C for further culture.

To verify the cytotoxicity of GNRs-PEG-TPEI during capture, cell membrane integrity and cell oxidative stress were further investigated.

4.11. Cellular Oxidative Stress Level Measurement. In the process of binding with cells, nanoprobes may disrupt the

https://doi.org/10.1021/acsomega.2c01494
ACS Omega 2022, 7, 18073−18084

oxidative balance of the cells, leading to an abnormal increase in intracellular ROS concentration and resulting in oxidative damage to targeted cells. The cell samples were added into an appropriate volume of DCFH-DA working solution (10 μM) and incubated at 37 °C for 1 h in the dark. DCFH-DA is a fluorescent probe that can pass through the cell membrane freely without fluorescence. After entering the cell, it can be hydrolyzed by intracellular esterase to form DCFH, which continues to be oxidized by ROS to a strong green fluorescence dye (DCF, maximum wavelengths of excitation/emission of 470/515 nm) that cannot penetrate the cell membrane. After incubation, DCFH-DA was removed. The cells were rinsed three times with PBS to fully remove the free DCFH-DA. The fluorescence images of the samples were captured with a fluorescence microscope (Eclipse Ts2 FL, Nikon, Japan). The fluorescence intensity of DCF and the intracellular ROS level were in a positive correlation manner.

4.12. Cell Viability Evaluation by LIVE/DEAD Staining. The cell viability of nanoprobe-captured and recultured cells was also assessed by double staining of living and dead cells. In this experiment, the LiveDye (maximum wavelengths of excitation/emission of 488/530 nm), a fluorescence dye for permeable cells, was used to stain the living cells. Meanwhile, the NucleiDye (maximum wavelengths of excitation/emission of 535/617 nm), a fluorescence dye for impermeable cells, was used to stain the dead cells.

The detection procedures were as follows: cell samples were added with an appropriate volume of LIVE/DEAD-dye working solution and incubated at 37 °C for 30 min in the dark. The LIVE/DEAD-dye working solution was removed. The cell surface was washed twice with PBS. The fluorescence image of the sample was captured with a fluorescence microscope (Eclipse Ts2 FL, Nikon, Japan).

4.13. Exploring the Genotoxicity of GNRs-PEG-TPEI. In order to explore the genotoxicity of GNRs-PEG-TPEI to cells, the mRNA expressions of some proto-oncogenes of MCF-7, HepG2, and Caco-2 after GNRs-PEG-TPEI capture and reculture were detected by real-time fluorescence quantitative PCR. At the same time, doxorubicin (DOX) was used as a model drug to investigate whether the gene regulation of cells was changed under the action of antitumor drugs. The adherent cells and suspension cells were captured and recultured, respectively. The cells were inoculated in a 6-well plate and placed in a 37 °C cell culture incubator for 24 h; then, the cell complete medium containing 1 μM DOX was added for further culture for 24 h. RNA was extracted and cDNA solution was obtained by a reverse transcription reaction. Three representative proto-oncogenes in MCF-7, HepG2, and Caco-2 cells were selected as the target genes, primers were designed, and GAPDH was selected as the reference gene. Finally, the relative expression levels of target genes were obtained by real-time fluorescence quantification.

4.14. Statistical Analysis. All data were processed using GraphPad Prism software. The error bars in each figure are indicated properly, which are presented as the standard deviation or the standard error of the mean (SEM). Statistical analysis was conducted using a paired or unpaired Student's *t*-test with GraphPad Prism software. Significance is represented on plots as ***$p < 0.001$, **$p < 0.01$, *$p < 0.05$, and ns for $p > 0.05$.

■ ASSOCIATED CONTENT

Supporting Information

The Supporting Information is available free of charge at https://pubs.acs.org/doi/10.1021/acsomega.2c01494.

Primer sequences, single-cell SERS spectra, and expression of proto-oncogenes (PDF)

■ AUTHOR INFORMATION

Corresponding Authors

Yang Liu − *School of Pharmaceutical Sciences (Shenzhen), Sun Yat-sen University, Guangzhou 510275, China;* orcid.org/0000-0001-9759-2417; Email: liuyang65@mail.sysu.edu.cn

Zhiyong Xie − *School of Pharmaceutical Sciences (Shenzhen), Sun Yat-sen University, Guangzhou 510275, China;* orcid.org/0000-0002-2147-6660; Email: xiezhy@mail.sysu.edu.cn

Authors

Xiaohan Kong − *School of Pharmaceutical Sciences (Shenzhen), Sun Yat-sen University, Guangzhou 510275, China*

Yangwen Sun − *School of Pharmaceutical Sciences (Shenzhen), Sun Yat-sen University, Guangzhou 510275, China*

Qian Zhang − *School of Pharmaceutical Sciences (Shenzhen), Sun Yat-sen University, Guangzhou 510275, China*

Siju Li − *School of Pharmaceutical Sciences (Shenzhen), Sun Yat-sen University, Guangzhou 510275, China*

Yizhen Jia − *School of Pharmaceutical Sciences (Shenzhen), Sun Yat-sen University, Guangzhou 510275, China*

Rui Li − *School of Pharmaceutical Sciences (Shenzhen), Sun Yat-sen University, Guangzhou 510275, China*

Complete contact information is available at: https://pubs.acs.org/10.1021/acsomega.2c01494

Author Contributions

†X.K. and Y.S. contributed equally to this work.

Notes

The authors declare no competing financial interest.

■ ACKNOWLEDGMENTS

This work was supported by the National Natural Science Foundation of China (grant numbers NSFC U1903211 and NSFC 82174104), the Guangdong Basic and Applied Basic Research Foundation (2021A1515010293), and the Technology & Innovation Commission of Shenzhen Municipality (JCYJ20190807153817192).

■ REFERENCES

(1) Lambert, A. W.; Pattabiraman, D. R.; Weinberg, R. A. Emerging Biological Principles of Metastasis. *Cell* **2017**, *168*, 670−691.

(2) Fidler, I. J. Critical Factors in the Biology of Human Cancer Metastasis: Twenty-eighth G. H. A. Clowes Memorial Award Lecture. *Cancer Res.* **1990**, *50*, 6130−6138.

(3) Fidler, I. J. Critical determinants of metastasis. *Semin. Cancer Biol.* **2002**, *12*, 89−96.

(4) Dominic, O. G.; McGarrity, T.; Dignan, M.; Lengerich, E. J. American College of Gastroenterology Guidelines for Colorectal Cancer Screening 2008. *Am. J. Gastroenterol.* **2009**, *104*, 2626−2627. Author reply: Rex, D. K.; Johnson, D. A.; Anderson, J. C.; Schoenfeld, P. S.; Burke, C. A.; Inadomi, J. M. Response to Meyer, Dominic et al., and Lin and Schembre. *Am. J. Gastroenterol.* **2009**, *104*, 2628−2629.

(5) Konishi, T.; Shimada, Y.; Hsu, M.; Tufts, L.; Jimenez-Rodriguez, R.; Cercek, A.; Yaeger, R.; Saltz, L.; Smith, J. J.; Nash, G. M.; Guillem, J. G.; Paty, P. B.; Garcia-Aguilar, J.; Gonen, M.; Weiser, M. R. Association of Preoperative and Postoperative Serum Carcinoembryonic Antigen and Colon Cancer Outcome. *JAMA Oncol.* **2018**, *4*, 309−315.
(6) Castro-Giner, F.; Aceto, N. Tracking cancer progression: from circulating tumor cells to metastasis. *Genome. Med.* **2020**, *12*, 31.
(7) Massague, J.; Obenauf, A. C. Metastatic colonization by circulating tumour cells. *Nature* **2016**, *529*, 298−306.
(8) Alix-Panabieres, C.; Pantel, K. Challenges in circulating tumour cell research. *Nat. Rev. Cancer* **2014**, *14*, 623−631.
(9) Marquette, C. H.; Boutros, J.; Benzaquen, J.; Ferreira, M.; Pastre, J.; Pison, C.; Padovani, B.; Bettayeb, F.; Fallet, V.; Guibert, N.; Basille, D.; Ilie, M.; Hofman, P.; Hofman, P.; Marquette, C. H.; Boutros, J.; Benzaquen, J.; Ferreira, M.; Pastre, J.; Pison, C.; Padovani, B.; Bettayeb, F.; Fallet, V.; Guibert, N.; Basille, D.; Ilie, M.; Hofman, V.; Hofman, P.; Israel-Biet, D.; Chabot, F.; Guillaumot, A.; Deslee, G.; Perotin, J. M.; Dury, S.; Mal, H.; Marceau, A.; Kessler, R.; Vergnon, J. M.; Pelissier, C.; di Palma, F.; Cuvelier, A.; Patout, M.; Bourdin, A.; Gamez, A. S.; Andrejak, C.; Poulet, C.; Francois, G.; Jounieaux, V.; Roche, N.; Jouneau, S.; Brinchault, G.; Bonniaud, P.; Zouak, A.; Scherpereel, A.; Baldacci, S.; Cortot, A.; Mornex, J. F.; Steenhouwer, F.; Leroy, S.; Berthet, J. P.; Fontas, E.; Bulsei, J.; Cruzel, C.; Pradelli, J.; Fontaine, M.; Maniel, C.; Griffonnet, J.; Butori, C.; Selva, E.; Poudenx, M.; AguilanIu, B.; Ferretti, G.; Arbib, F.; Briault, A.; Toffart, A. C.; Dahalani, R.; Destors, M.; Chanez, P.; Greillier, L.; Astoul, P.; Barlesi, F.; Gaubert, J. Y.; Mazières, J.; Marchand-Adam, S.; Cadranel, J.; Chaabane, N.; Izadifar, A.; Rosencher, L.; Ruppert, A. M.; Vieira, T.; Mathiot, N. Circulating tumour cells as a potential biomarker for lung cancer screening: a prospective cohort study. *Lancet Respir. Med.* **2020**, *8*, 709−716.
(10) Pantel, K.; Brakenhoff, R. H.; Brandt, B. Detection, clinical relevance and specific biological properties of disseminating tumour cells. *Nat. Rev. Cancer* **2008**, *8*, 329−340.
(11) Kim, S. I.; Jung, H.-i. Circulating Tumor Cells: Detection Methods and Potential Clinical Application in Breast Cancer. *Int. J. Breast Cancer* **2010**, *13*, 125.
(12) Woo, D.; Yu, M. Circulating tumor cells as "liquid biopsies" to understand cancer metastasis. *Transl. Res.* **2018**, *201*, 128−135.
(13) Paterlini-Brechot, P.; Benali, N. L. Circulating tumor cells (CTC) detection: clinical impact and future directions. *Cancer Lett.* **2007**, *253*, 180−204.
(14) Lin, H. K.; Zheng, S.; Williams, A. J.; Balic, M.; Groshen, S.; Scher, H. I.; Fleisher, M.; Stadler, W.; Datar, R. H.; Tai, Y. C.; Cote, R. J. Portable filter-based microdevice for detection and characterization of circulating tumor cells. *Clin. Cancer Res.* **2010**, *16*, 5011−5018.
(15) Huang, S. B.; Wu, M. H.; Lin, Y. H.; Hsieh, C. H.; Yang, C. L.; Lin, H. C.; Tseng, C. P.; Lee, G. B. High-purity and label-free isolation of circulating tumor cells (CTCs) in a microfluidic platform by using optically-induced-dielectrophoretic (ODEP) force. *Lab Chip* **2013**, *13*, 1371−1383.
(16) den Toonder, J. Circulating tumor cells: the Grand Challenge. *Lab Chip* **2011**, *11*, 375.
(17) De Giorgi, V.; Pinzani, P.; Salvianti, F.; Panelos, J.; Paglierani, M.; Janowska, A.; Grazzini, M.; Wechsler, J.; Orlando, C.; Santucci, M.; Lotti, T.; Pazzagli, M.; Massi, D. Application of a filtration- and isolation-by-size technique for the detection of circulating tumor cells in cutaneous melanoma. *J. Invest. Dermatol.* **2010**, *130*, 2440−2447.
(18) Fang, J. S.; Gillies, R. D.; Gatenby, R. A. Adaptation to hypoxia and acidosis in carcinogenesis and tumor progression. *Semin. Cancer Biol.* **2008**, *18*, 330−337.
(19) Kroemer, G.; Pouyssegur, J. Tumor cell metabolism: cancer's Achilles' heel. *Cancer Cell* **2008**, *13*, 472−482.
(20) Boroughs, L. K.; DeBerardinis, R. J. Metabolic pathways promoting cancer cell survival and growth. *Nat. Cell Biol.* **2015**, *17*, 351−359.
(21) Gatenby, R. A.; Gawlinski, E. T.; Gmitro, A. F.; Kaylor, B.; Gillies, R. D. Acid-mediated tumor invasion: a multidisciplinary study. *Cancer Res.* **2006**, *66*, 5216−5223.
(22) Lunt, S. Y.; Vander Heiden, M. G. Aerobic glycolysis: meeting the metabolic requirements of cell proliferation. *Annu. Rev. Cell Dev. Biol.* **2011**, *27*, 441−464.
(23) Estrella, V.; Chen, T.; Lloyd, M.; Wojtkowiak, J.; Cornnell, H. H.; Ibrahim-Hashim, A.; Bailey, K.; Balagurunathan, Y.; Rothberg, J. M.; Sloane, B. F.; Johnson, J.; Gatenby, R. A.; Gillies, R. D. Acidity generated by the tumor microenvironment drives local invasion. *Cancer Res.* **2013**, *73*, 1524−1535.
(24) Chen, B.; Le, W.; Wang, Y.; Li, Y.; Wang, D.; Ren, L.; Lin, B.; Cui, S.; Hu, J. J.; Hu, Y.; Yang, P.; Ewing, R. C.; Shi, D.; Cui, S. Targeting Negative Surface Charges of Cancer Cells by Multifunctional Nanoprobes. *Theranostics* **2016**, *6*, 1887−1898.
(25) DeBerardinis, R. J.; Lum, J. J.; Hatzivassiliou, G.; Thompson, C. B. The biology of cancer: metabolic reprogramming fuels cell growth and proliferation. *Cell Metab.* **2008**, *7*, 11−20.
(26) Yoong, H. J.; Kozminsky, M.; Nagrath, S. Emerging role of nanomaterials in circulating tumor cell isolation and analysis. *ACS Nano* **2014**, *8*, 1995−2017.
(27) Wang, L.; Asghar, W.; Demirci, U.; Wan, Y. Nanostructured substrates for isolation of circulating tumor cells. *Nano Today* **2013**, *8*, 347−387.
(28) Zhang, P.; Chen, L.; Xu, T.; Liu, H.; Liu, X.; Meng, J.; Yang, G.; Jiang, L.; Wang, S. Programmable fractal nanostructured interfaces for specific recognition and electrochemical release of cancer cells. *Adv. Mater.* **2013**, *25*, 3566−3570.
(29) Jan, Y. J.; Chen, J. F.; Zhu, Y.; Lu, Y. T.; Chen, S. H.; Chung, H.; Smalley, M.; Huang, Y. W.; Dong, J.; Yu, H.; Tomlinson, J. S.; Hou, G.; Agopian, V. G.; Posadas, E. M.; Tseng, H. R. NanoVelcro rare-cell assays for detection and characterization of circulating tumor cells. *Adv. Drug Delivery Rev.* **2018**, *125*, 78−93.
(30) Zhou, W.; Gao, X.; Liu, D.; Chen, X. Gold Nanoparticles for In Vitro Diagnostics. *Chem. Rev.* **2015**, *115*, 10575−10636.
(31) Gao, Z.; Ye, H.; Tang, D.; Tao, J.; Habibi, S.; Minerick, A.; Tang, D.; Xia, X. Platinum-Decorated Gold Nanoparticles with Dual Functionalities for Ultrasensitive Colorimetric in Vitro Diagnostics. *Nano Lett.* **2017**, *17*, 5572−5579.
(32) Li, N.; Zhao, P.; Astruc, D. Anisotropic gold nanoparticles: synthesis, properties, applications, and toxicity. *Angew. Chem., Int. Ed.* **2014**, *53*, 1756−1789.
(33) Hu, M.; Chen, J. F.; Li, J. Y.; Au, L.; Hartland, G. V.; Li, C.; Marqueze, M.; Xia, Y. Gold nanostructures: engineering their plasmonic properties for biomedical applications. *Chem. Soc. Rev.* **2006**, *35*, 1084.
(34) Lee, S. A.; Link, S. Chemical Interface Damping of Surface Plasmon Resonances. *Acc. Chem. Res.* **2021**, *54*, 1950−1960.
(35) Nie, S.; Emory, S. R. Probing Single Molecules and Single Nanoparticles by Surface-Enhanced Raman Scattering. *Science* **1997**, *275*, 1102−1106.
(36) Qiu, Y.; Liu, Y.; Wang, L.; Xu, L.; Bai, R.; Ji, Y.; Wu, X.; Zhao, Y.; Li, C.; Chen, C. Surface chemistry and aspect ratio mediated cellular uptake of Au nanorods. *Biomaterials* **2010**, *31*, 7606−7619.
(37) Xiao, Z.; Ji, C.; Shi, J.; Pridgen, E. M.; Frieder, J.; Wu, J.; Farokhzad, O. C. DNA self-assembly of targeted near-infrared-responsive gold nanoparticles for cancer thermo-chemotherapy. *Angew. Chem., Int. Ed.* **2012**, *51*, 11853−11857.
(38) Xu, W.; Qian, J.; Hou, G.; Suo, A.; Wang, D.; Wang, D.; Sun, T.; Yang, G.; Wan, X.; Yao, Y. Hyaluronic Acid-Functionalized Gold Nanorods with pH/NIR Dual-Responsive Drug Release for Synergetic Targeted Photothermal Chemotherapy of Breast Cancer. *ACS Appl. Mater. Interfaces* **2017**, *9*, 36533−36547.
(39) Chen, Y. S.; Zhao, Y.; Yoon, S. J.; Gambhir, S. S.; Emelianov, S. Miniature gold nanorods for photoacoustic molecular imaging in the second near-infrared optical window. *Nat. Nanotechnol.* **2019**, *14*, 465−472.

https://doi.org/10.1021/acsomega.2c01494
ACS Omega 2022, 7, 18073−18084

(40) Zhang, W.; Guo, Z.; Huang, D.; Liu, Z.; Guo, X.; Zhong, H. Synergistic effect of chemo-photothermal therapy using PEGylated graphene oxide. *Biomaterials* **2011**, *32*, 8555−8561.
(41) Wang, D.; Xu, Z.; Yu, H.; Chen, X.; Feng, B.; Cui, Z.; Lin, B.; Yin, Q.; Zhang, C.; Chen, Z.; Wang, J.; Zhang, W.; Li, Y. Treatment of metastatic breast cancer by combination of chemotherapy and photothermal ablation using doxorubicin-loaded DNA wrapped gold nanorods. *Biomaterials* **2014**, *35*, 8374−8384.
(42) Li, C.; Wu, C.; Zheng, J.; Lai, J.; Zhang, C.; Zhao, Y. LSPR sensing of molecular biothiols based on noncoupled gold nanorods. *Langmuir* **2010**, *26*, 9130−9135.
(43) Wolfbeis, O. S. An overview of nanoparticles commonly used in fluorescent bioimaging. *Chem. Soc. Rev.* **2015**, *44*, 4743−4768.
(44) Lim, X. The nanolight revolution is coming. *Nature* **2016**, *531*, 26−28.
(45) Baig, M. Z. K.; Prusti, B.; Roy, D.; Chakravarty, M. Positional Variation of Monopyridyl-N in Unsymmetrical Anthracenyl π-Conjugates: Difference between Solution- and Aggregate-State Emission Behavior. *ACS Omega* **2019**, *4*, 5052−5063.
(46) Hu, Q.; Gao, M.; Feng, G.; Liu, B. Mitochondria-targeted cancer therapy using a light-up probe with aggregation-induced-emission characteristics. *Angew. Chem., Int. Ed.* **2014**, *53*, 14225−14229.
(47) Cai, X.; Liu, B. Aggregation-Induced Emission: Recent Advances in Materials and Biomedical Applications. *Angew. Chem., Int. Ed.* **2020**, *59*, 9868−9886.
(48) Li, S.; He, J.; Xu, Q. H. Aggregation of Metal-Nanoparticle-Induced Fluorescence Enhancement and Its Application in Sensing. *ACS Omega* **2020**, *5*, 41−48.
(49) Chua, M. H.; Zhou, H.; Lin, T. T.; Wu, J.; Xu, J. Triphenylethylene- and Tetraphenylethylene-Functionalized 1,3-Bis-(pyrrol-2-yl)squaraine Dyes: Synthesis, Aggregation-Caused Quenching to Aggregation-Induced Emission, and Thiol Detection. *ACS Omega* **2018**, *3*, 16424−16435.
(50) Kostarelos, K.; Lacerda, L.; Pastorin, G.; Wu, C.; Wieckowski, S.; Luangsivilay, J.; Godefroy, S.; Pantarotto, D.; Briand, J. P.; Muller, S.; Prato, M.; Bianco, A. Cellular uptake of functionalized carbon nanotubes is independent of functional group and cell type. *Nat. Nanotechnol.* **2007**, *2*, 108−113.
(51) Marquis, B. J.; Love, S. A.; Braun, K. L.; Haynes, C. L. Analytical methods to assess nanoparticle toxicity. *Analyst* **2009**, *134*, 425−439.
(52) Apel, K.; Hirt, H. Reactive oxygen species: metabolism, oxidative stress, and signal transduction. *Annu. Rev. Plant Biol.* **2004**, *55*, 373−399.
(53) Li, Y.; Rodrigues, J.; Tomás, H. Injectable and biodegradable hydrogels: gelation, biodegradation and biomedical applications. *Chem. Soc. Rev.* **2012**, *41*, 2193−2221.

https://doi.org/10.1021/acsomega.2c01494
ACS Omega 2022, 7, 18073−18084